

Site-Selective Oxygen Vacancy Formation Derived from the Characteristic Crystal Structures of Sn-Nb Complex Oxides

Akane Samizo^{1,2,}, Makoto Minohara², Naoto Kikuchi², Kyoko K. Bando³, Yoshihiro Aiura², Ko Mibu⁴, and Keishi Nishio¹*

¹Department of Materials Science and Technology, Tokyo University of Science, Katsushika 125-8585, Japan

²Research Institute for Advanced Electronics and Photonics, National Institute of Advanced Industrial Science and Technology (AIST), Tsukuba, Ibaraki 305-8568, Japan

³Nanomaterials Research Institute, National Institute of Advanced Industrial Science and Technology (AIST), Tsukuba, Ibaraki 305-8565, Japan

⁴Department of Physical Science and Engineering, Nagoya Institute of Technology, Nagoya 466-8555, Japan

Divalent stannous oxide, oxide semiconductor, *p*-type, oxygen vacancy, EXAFS, Rietveld analysis

ABSTRACT: Divalent tin oxides have attracted considerable attention as novel *p*-type oxide semiconductors, which are essential for realizing future oxide electronic devices. Recently, *p*-type

$\text{Sn}_2\text{Nb}_2\text{O}_7$ and SnNb_2O_6 were developed; however, enhanced hole mobility by reducing defect concentrations is required for practical use. In this work, we investigate the correlation between the formation of oxygen vacancy ($V_{\text{O}}^{\cdot\cdot}$), which may reduce the hole-generation efficiency and hole mobility, and the crystal structure in Sn-Nb complex oxides. Extended X-ray absorption fine structure spectroscopy and Rietveld analysis of x-ray diffraction revealed the preferential formation of $V_{\text{O}}^{\cdot\cdot}$ at the O site bonded to the Sn ions in both the tin niobates. Moreover, a large amount of $V_{\text{O}}^{\cdot\cdot}$ around the Sn ions were found in the *p*-type $\text{Sn}_2\text{Nb}_2\text{O}_7$, thereby indicating the effect of $V_{\text{O}}^{\cdot\cdot}$ to the low hole-generation efficiency. The dependence of the formation of $V_{\text{O}}^{\cdot\cdot}$ on the crystal structure can be elucidated from the Sn-O bond strength that is evaluated based on the bond valence sum and Debye temperature. The differences in the bond strengths of the two Sn-Nb complex oxides are correlated through the steric hindrance of Sn^{2+} with asymmetric electron density distribution. This suggests the importance of the material design with a focus on the local structure around the Sn ions to prevent the formation of $V_{\text{O}}^{\cdot\cdot}$ in *p*-type Sn^{2+} oxides.

INTRODUCTION

Oxide semiconductors with high electrical conductivity and transparency have attracted significant attention owing to their application in several technologies such as thin-film solar cells and/or touch screens. However, most of the existing oxide semiconductors are *n*-type oxides, such as Sn-doped In_2O_3 (ITO) and $\text{InGaO}_3(\text{ZnO})_5$ (IGZO) [1], and the lack of practical *p*-type oxide semiconductors limits their applications to unipolar devices. Fabrications of the *p-n* junctions, as same as technologies for Si semiconductors, will lead to more energy saving, and more complex transparent devices, and thus it is important to develop *p*-type oxides for the future “oxide electronics” [2].

One of the intrinsic problems in the development of *p*-type oxide semiconductors is the low hole mobility due to a flat valence band maximum composed of an O 2p orbital [3, 4]. To reduce strong localization of holes, modifying the valence band structure by hybridization of the O 2p orbital with a metallic s or d orbital is theoretically suggested [3]. Because the s orbital has an electron density with a large spatial spread and strong interactions with the neighboring atoms, the degree of valence band dispersion is particularly large for the s orbital-based materials. Thus, oxides including cations with ns^2 electronic configuration (such as Sn^{2+} , Pb^{2+} , and Bi^{3+}) have attracted attention as new candidates for *p*-type oxides [3-7]. This approach was demonstrated through the fabrication of SnO films with a hole mobility of $\sim 21 \text{ cm}^2\text{V}^{-1}\text{s}^{-1}$ [8-11]. However, because SnO has an indirect band gap of 0.7 eV [9], it is not suitable for future transparent device applications. For realizing both high hole mobility and transparency, *p*-type tin oxides with wide band gaps are required.

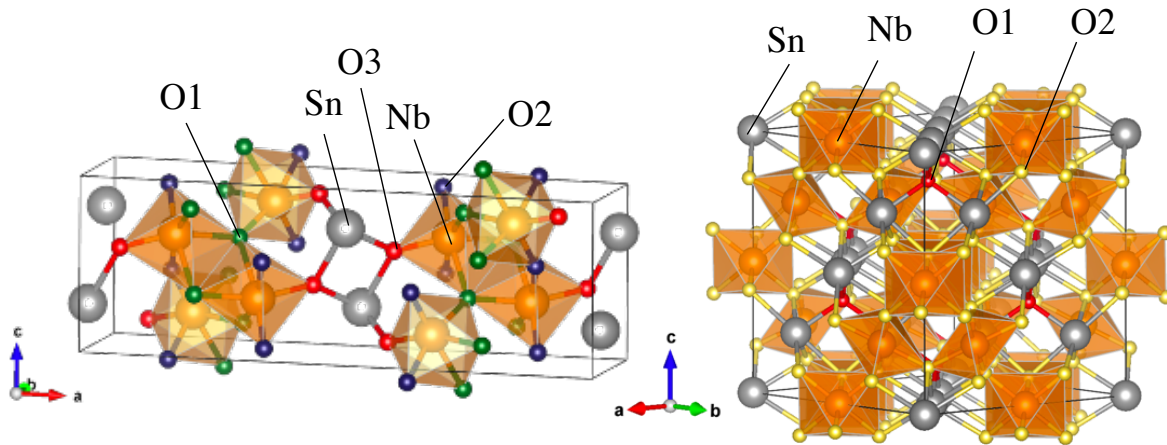
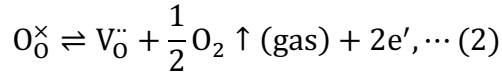
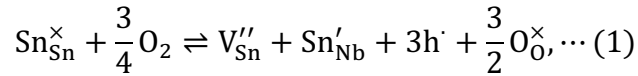


Figure 1. Crystal structures of SnNb_2O_6 (left) and $\text{Sn}_2\text{Nb}_2\text{O}_7$ (right). The information for each site is provided in previous reports [13,14]. The O ions are denoted in different color based on the site. The closest O site to Sn (O3 and O1 for SnNb_2O_6 and $\text{Sn}_2\text{Nb}_2\text{O}_7$, respectively) is denoted in red.

Recently, we developed novel *p*-type Sn²⁺ oxides, SnNb₂O₆ and Sn₂Nb₂O₇, with a band gap of 2.4 eV (Fig. 1) [13,14]. Although their valence band is composed of Sn 5s orbital, they showed low hole mobility of 0.03–0.4 cm²V⁻¹s⁻¹ so far [12-14]. In general, since structural defects act as the scattering centers for electrons (holes), the mobility declines with the increase of the defect density, and hence, the reduction of these defects is a common strategy for improving hole mobility [18]. By the same time, the carriers are generated by the defect formations, therefore, a high carrier generation efficiency of the donor (acceptor) is required to improve the hole mobility for practical applications. Thus, it is important to focus on the underlying mechanism of the defect formations. The above-mentioned Sn-Nb complex oxides are known to have three native defects: the Sn vacancy (V_{Sn}^{''}), the Sn⁴⁺ substitutional defect at the Nb⁵⁺ site (Sn'_{Nb}), and oxygen vacancy (V_O^{••}) [19-24]. The charge carriers are generated by the defect formations, as shown below,



where Sn_{Sn}[×] and O_O[×] are Sn²⁺ at the Sn site and O²⁻ at the O site. These defect formations occur simultaneously during sample fabrication. Since the Eqs. (1) and (2) generate holes and electrons, respectively, the balance of these defect formations determines the carrier type and density. In fact, the carrier type of these Sn-Nb complex oxides can be manipulated by controlling the annealing conditions [12,13]. The net carrier density (*n_h* and *n_e* for hole and electron densities, respectively) and Sn'_{Nb} density (*N_{Sn',Nb}*) of SnNb₂O₆ and Sn₂Nb₂O₇ for both the *p*- and *n*-types are summarized in Table 1. With the change in the carrier type from *p*-type to *n*-type, the amount of Sn'_{Nb} clearly decreases. Here, we note that the amount of net carrier of *p*-type samples cannot be quantitatively

described by the amount of Sn'_{Nb} ; the hole densities are two or three orders magnitude lower than Sn'_{Nb} density. The degree of such mismatch between hole and Sn'_{Nb} density of SnNb_2O_6 is different from that of $\text{Sn}_2\text{Nb}_2\text{O}_7$. When the hole-generation efficiency (η_{Hole}) is defined by $n_h / 3N_{\text{Sn}'_{\text{Nb}}}$ based on Eq. (1), the η_{Hole} value of SnNb_2O_6 is found to be three orders of magnitude higher than that of $\text{Sn}_2\text{Nb}_2\text{O}_7$. Considering the fact that the Sn-Nb complex oxides are annealed in reductive atmosphere to prevent oxidative decompositions, it is naturally expected that the charge compensation was occurred by the formation of large amounts of $V_{\text{O}}^{\bullet\bullet}$ as shown in Eqs. (2). Thus, in order to clarify the mechanism of appearing *p*-type carriers in electrical properties, the $V_{\text{O}}^{\bullet\bullet}$ formation has to be considered. In this study, we investigated the formation of $V_{\text{O}}^{\bullet\bullet}$ in SnNb_2O_6 and $\text{Sn}_2\text{Nb}_2\text{O}_7$ through extended X-ray absorption fine structure (EXAFS) spectroscopy. We found that $V_{\text{O}}^{\bullet\bullet}$ can be formed preferentially around the Sn ions for both SnNb_2O_6 and $\text{Sn}_2\text{Nb}_2\text{O}_7$. In addition, it was revealed that the degree of the structural disorders which derived from the $V_{\text{O}}^{\bullet\bullet}$ formation was higher in *p*-type $\text{Sn}_2\text{Nb}_2\text{O}_7$ with low η_{Hole} than that in the *p*-type SnNb_2O_6 . These findings can be well explained based on the Sn-O bond strength in the two different crystal structures.

Table 1 Hole density (n_h), electron density (n_e), Sn'_{Nb} density ($N_{\text{Sn}'_{\text{Nb}}}$), and hole-generation efficiencies (η_{Hole}) in SnNb_2O_6 and $\text{Sn}_2\text{Nb}_2\text{O}_7$. The value of $N_{\text{Sn}'_{\text{Nb}}}$ of *n*-type SnNb_2O_6 is lower than the Sn^{4+} detection limit of Mössbauer spectroscopy.

	Carrier type	n_h (n_e) [cm^{-3}]	$N_{\text{Sn}'_{\text{Nb}}}$ [cm^{-3}]	η_{Hole}
SnNb_2O_6	<i>p</i> -type	3.7×10^{18}	8.6×10^{19}	1.4×10^{-2}
	<i>n</i> -type	7.5×10^{15}	0.0	-
$\text{Sn}_2\text{Nb}_2\text{O}_7$	<i>p</i> -type	2.5×10^{17}	1.7×10^{21}	4.9×10^{-5}
	<i>n</i> -type	4.9×10^{15}	7.3×10^{20}	-

EXPERIMENTAL METHOD

Sample Preparation

$\text{Sn}_2\text{Nb}_2\text{O}_7$ and SnNb_2O_6 were prepared through solid-state reactions. The starting materials used were SnO (Kojundo Chemical Laboratory; purity, 99.5 %) and Nb_2O_5 (Kojundo Chemical Laboratory; purity, 99.9 %). They were mixed in an agate mortar with ethanol and dried in air for 24 h. The mixed powder was then calcined at 1173 K in an alumina tube furnace under N_2 at a flow rate of 150 ml min^{-1} . The synthesized samples were annealed to obtain *p*-type and *n*-type conductivities as follows. The calcined powder was ground again in an agate mortar, followed by mixing with a polyvinyl alcohol (PVA) aqueous solution (PVA: 2 wt.% to the sample) and ethanol. After air-drying for 24 h, the dried samples were sieved to obtain narrow sieve fractions $< 212 \mu\text{m}$. The obtained powder was pressed isostatically at 290 MPa to form discs of 12 mm diameter. The sample disks were annealed in the tube furnace under each of following heating conditions: 1023 K under a N_2 atmosphere at a flow rate of 50 ml min^{-1} for *p*-type $\text{Sn}_2\text{Nb}_2\text{O}_7$ and SnNb_2O_6 , 1473 K under the N_2 atmosphere at a flow rate of 150 ml min^{-1} for *n*-type $\text{Sn}_2\text{Nb}_2\text{O}_7$, and 1473 K under the N_2 atmosphere at a flow rate of 100 ml min^{-1} for *n*-type SnNb_2O_6 .

Structural Characterization

The crystal structure was confirmed by X-ray diffraction (XRD), which was conducted using the Bragg–Brentano configuration with Cu $K\alpha$ radiation (PANalytical, X'Pert Pro MPD). The structure parameters of $\text{Sn}_2\text{Nb}_2\text{O}_7$ were refined by the Rietveld analysis using the RIETAN-FP software [25]. The crystal structure was obtained by the VESTA software [26].

The local crystal structures were investigated by EXAFS measurements. The EXAFS spectra of all the samples were measured by the transmission mode at 40 K. The Sn K-edge and Nb K-edge spectra were observed at the beamline AR-NW10A of the Photon Factory Advanced Ring (PF-

AR) and BL-9C of Photon Factory, KEK [27]. The EXAFS spectra were Fourier-transformed using the Hanning window function within the k range of 3.0–14.0 \AA^{-1} for the Sn K-edge, Nb K-edge of SnNb_2O_6 , and Nb K-edge of $\text{Sn}_2\text{Nb}_2\text{O}_7$, and 3.0–13.0 \AA^{-1} for the Sn K-edge of $\text{Sn}_2\text{Nb}_2\text{O}_7$. The data processing of the EXAFS spectra was performed using Athena [28].

The ^{119}Sn Mössbauer spectroscopy was conducted by the conventional transmission method under the same experimental geometry at 78 and 300 K. The powder samples were mixed with silicone grease and plastered on pure Al foil to eliminate any orientation effect. The range of the Doppler velocity of the $\text{Ca}^{119\text{m}}\text{SnO}_3$ source was set to $\pm 8 \text{ mm s}^{-1}$. The peak position was calibrated using a CaSnO_3 reference.

RESULTS AND DISCUSSIONS

Comparing the formation of oxygen vacancies through crystal structure analysis

Before discussing the possible $V_{\text{O}}^{\bullet\bullet}$ formation and its crystal structure dependency, we provide an experimental evidence of the comparable crystalline quality between the SnNb_2O_6 and $\text{Sn}_2\text{Nb}_2\text{O}_7$ samples. Figures S1(a) and (b) show the XRD patterns of the p - and n -type samples (see supplementary section S1). The Bragg peaks assigned for SnNb_2O_6 (JCPDS : 98-020-2827) and $\text{Sn}_2\text{Nb}_2\text{O}_7$ (JCPDS : 98-027-9575) were observed to be sharp. This indicates sufficient crystalline quality to perform the EXAFS spectroscopy and discuss the possible local disorder in the crystal structure due to the formation of $V_{\text{O}}^{\bullet\bullet}$.

The Fourier transforms (FT) of the Sn K-edge and Nb K-edge EXAFS spectra of SnNb_2O_6 are shown in Figs. 2 (a) and (b), respectively. In Fig. 2(a), the peak between 1.5 and 1.7 \AA in the FT of the Sn K-edge EXAFS spectra corresponds to the first-neighbor Sn-O bond. The peak intensity of the Sn-O bond in the n -type sample is distinctly weaker than that in the p -type sample. Here,

the spectral intensities of the FT feature mainly reflect the coordination number (N_j) of the absorbing atom and the Debye Waller factor (σ_j) of the scattering atom, which corresponds to the magnitude of thermal vibrations depending on the crystalline quality. Considering the higher annealing temperature of the *n*-type sample than the *p*-type one ($|\Delta T| = 450$ K), σ_j of the *n*-type sample is naturally expected to be lower than that of the *p*-type one. Namely, the FT magnitude of the *n*-type sample could be stronger than that of the *p*-type one; however, this contradicts the experimental findings. Therefore, the significant decrease in the Sn-O peak intensity can be assumed to be a decrease in N_j , that is, formation of V_{O} . Simultaneously, we notice that the EXAFS oscillation becomes unclear for the *n*-type sample (inset of Fig. 2(a)), suggesting the formation of structural disorder around the Sn ions.

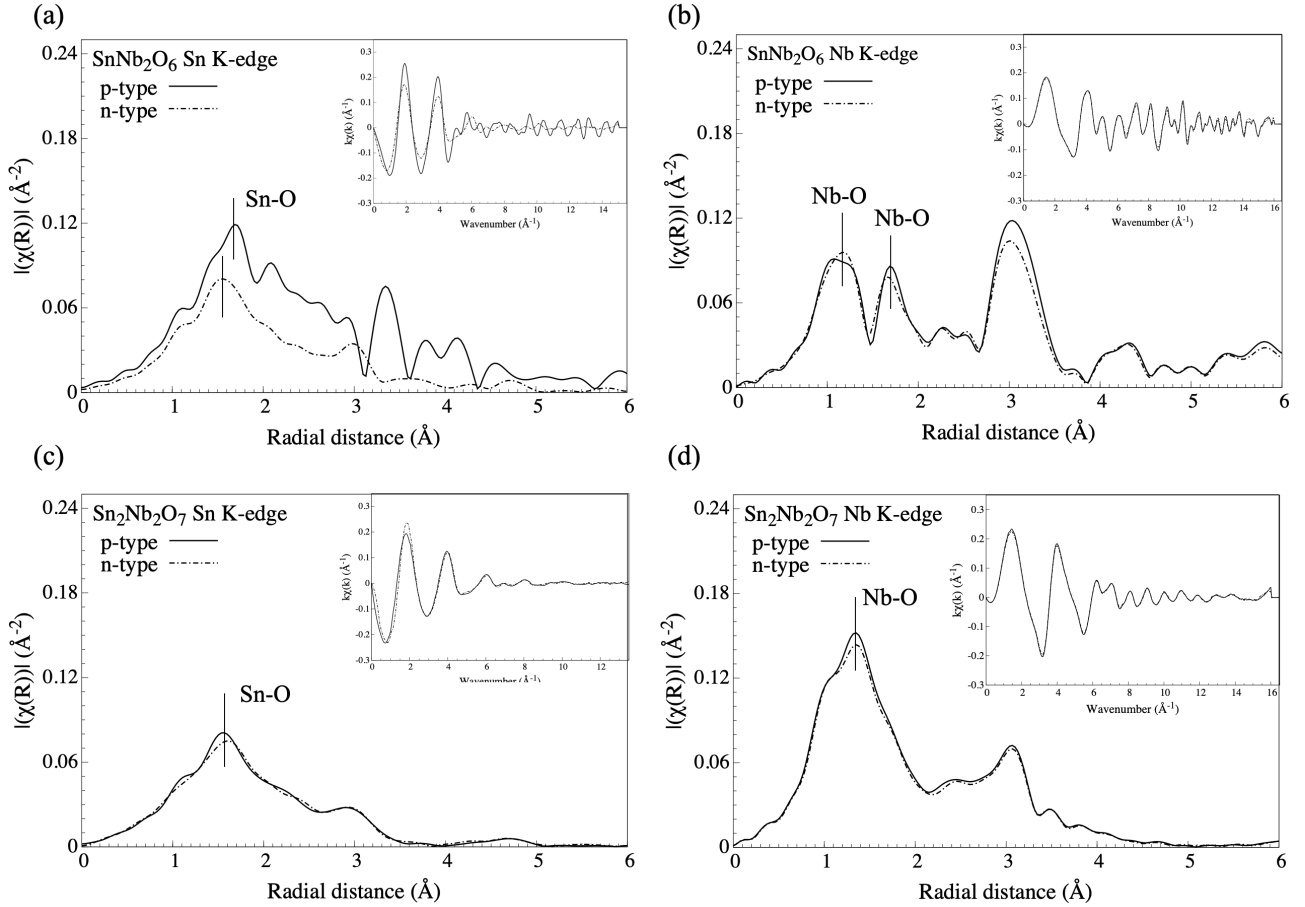


Figure 2. Extracted EXAFS oscillations (inset) and the associated k -weighted Fourier transform of (a) Sn K-edge, (b) Nb K-edge of SnNb_2O_6 , and (c) Sn K-edge, (d) Nb K-edge of $\text{Sn}_2\text{Nb}_2\text{O}_7$. The p - and n -type samples are denoted by solid and dotted lines, respectively.

In contrast, in Fig. 2 (b), two peaks are observed in the FT of the Nb K-edge EXAFS spectra for radial distance (r) < 2 Å. However, a slightly complex behavior is observed in the FT spectra of the Nb K-edge compared to that of the Sn K-edge; the intensity of the first shell ($r = 1.1$ Å) for the n -type sample seems to be stronger than that for the p -type one; however, the second shell ($r = 1.7$ Å) shows an opposite behavior. As mentioned above, the FT magnitude of the n -type sample will

be higher than that of *p*-type one, when we assume a low σ_j values with higher annealing temperatures for the *n*-type samples. Thus, this complex feature could reflect the decrease in N_j . It is noteworthy that the decrease in the intensity is significant for the Sn K-edge as compared to Nb K-edge. From the spectral calculations using *FEFF* program [29, 30], the first metal-oxide scattering peaks in the Sn K-edge ($r \sim 1.5 \text{ \AA}$) and Nb K-edge ($r \sim 1.8 \text{ \AA}$) EXAFS spectra mainly originate from the Sn-O3 bonds and Nb-O1 and Nb-O2 bonds, respectively (see supplementary S2). Given the large decrease in the intensity of the FT EXAFS spectra for the Sn K-edge, we can consider that V_{O}^{\bullet} is preferentially formed at O3 sites rather than at O1 and/or O2 sites. The site-selective V_{O}^{\bullet} formation is consistent with the findings in the Rietveld analysis of the XRD patterns (see supplementary S3).

Figures 2 (c) and (d) show the FT of the Sn K-edge and Nb K-edge EXAFS spectra of $\text{Sn}_2\text{Nb}_2\text{O}_7$, respectively. The intensity of the *n*-type sample for both the FT spectra is slightly weaker than that of the *p*-type one, suggesting larger formation of V_{O}^{\bullet} for the *n*-type sample. Initially, negligible differences are observed between the Sn K-edge and Nb K-edge; the preferential formation of V_{O}^{\bullet} for *n*-type is not evident for $\text{Sn}_2\text{Nb}_2\text{O}_7$ as it is for SnNb_2O_6 . However, upon closer look at the EXAFS oscillations at wavenumber (k) > 6 \AA^{-1} , Sn K-edge EXAFS oscillation is unclear for both *p*-type and *n*-type $\text{Sn}_2\text{Nb}_2\text{O}_7$ (inset of Fig. 2(c)), which is similar to the behavior observed for *n*-type SnNb_2O_6 . This suggests that the local structural disorder occurs around the Sn ions. In the crystal structure of $\text{Sn}_2\text{Nb}_2\text{O}_7$, there are two different oxygen sites named O1 and O2, where the former and latter correspond to the oxygen sites closest to Sn and Nb, respectively. Considering its structural analogy to SnNb_2O_6 , the findings from EXAFS oscillations suggest that there are large amounts of V_{O}^{\bullet} at O1 in $\text{Sn}_2\text{Nb}_2\text{O}_7$.

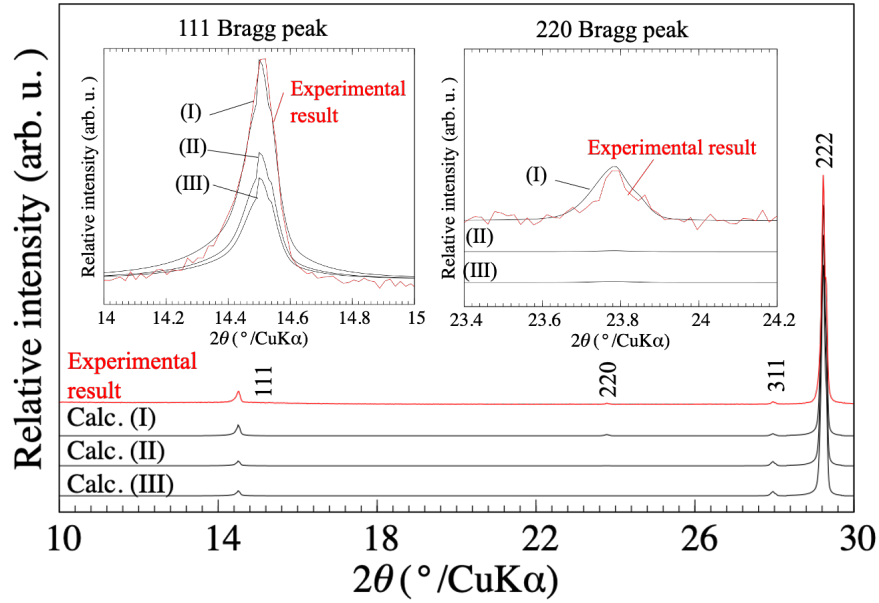


Figure 3. Comparison of experimental result and calculated XRD patterns of *p*-type $\text{Sn}_2\text{Nb}_2\text{O}_7$ based on the (I) O1-deficient model, (II) ideal model without V_{O}^{\bullet} , and (III) O2-deficient model. The insets show the magnification around 111 (left, $2\theta = 14.0\text{--}15.0^\circ$) and 220 (right, $2\theta = 23.4\text{--}24.2^\circ$) Bragg peaks. The intensity was normalized as the relative intensity, which is the ratio of the intensities of each Bragg peak to the highest 222 peak intensity.

Again, the Rietveld analysis supports the large V_{O}^{\bullet} formation at O1 site in $\text{Sn}_2\text{Nb}_2\text{O}_7$ [14]. Figure 3 shows a comparison of the experimental result with the calculated XRD patterns of *p*-type $\text{Sn}_2\text{Nb}_2\text{O}_7$ (the structural parameters for the calculated patterns are shown under section S4). The intensity is normalized by the intensity of the 222 Bragg peak. Here, the calculated patterns (I), (II), and (III) indicate the O1-deficient model, ideal model without V_{O}^{\bullet} formation, and O2-deficient model, respectively. The insets show the magnification around the 111 ($2\theta = 14.0\text{--}15.0^\circ$) and 220 ($2\theta = 23.4\text{--}24.2^\circ$) Bragg peaks. As for the 111 Bragg peak, the O1-deficient model shows the

highest intensity. Moreover, the 220 Bragg peak can be clearly observed only in pattern (I). These characteristics in pattern (I) are consistent with the experimental result, which indicates the site-selective $V_{\text{O}}^{\ddot{}}$ formations at the O1 site. Therefore, the structural disorder, which is potentially triggered by the $V_{\text{O}}^{\ddot{}}$ formation, occurs preferentially around the Sn ions. These findings are supported by our preliminary calculations on the defect formation energy [16].

Further, we focus on the difference between p -type SnNb_2O_6 and p -type $\text{Sn}_2\text{Nb}_2\text{O}_7$. As shown in Figs. 2(a) and (c), the peak intensity of Sn-O bonds in FT spectra for p -type $\text{Sn}_2\text{Nb}_2\text{O}_7$ is lower than that for p -type SnNb_2O_6 and comparable with that of oxygen-deficient n -type SnNb_2O_6 . This can also be observed in the EXAFS oscillations as mentioned above. These findings strongly suggest large amount of $V_{\text{O}}^{\ddot{}}$ formation around the Sn ions in not only for n -type $\text{Sn}_2\text{Nb}_2\text{O}_7$ but also p -type one. Therefore, poor η_{Hole} in p -type $\text{Sn}_2\text{Nb}_2\text{O}_7$ occurs due to the larger amount of $V_{\text{O}}^{\ddot{}}$ formation than in p -type SnNb_2O_6 .

Strength of Sn-O bond in Sn-Nb complex oxides

To understand the different $V_{\text{O}}^{\ddot{}}$ formations around the Sn ions between SnNb_2O_6 and $\text{Sn}_2\text{Nb}_2\text{O}_7$, we note the Sn-O bond strength in each structure. Bond valence sum (BVS) is a suitable indicator of the bond strength [31]. The bond valence S_{ij} is directly related to the strength of the Sn-O bond and inversely with the bond length [32,33]. It can be approximated as

$$S_{ij} = \exp\left(\frac{R_0 - R_{ij}}{B}\right), \quad \dots (3)$$

where R_0 is the bond valence parameter, 1.984 Å for Sn-O bond and 1.916 Å for Nb-O bond, R_{ij} and B are the actual bond length and 0.37 which is a constant independent of an element, respectively [34, 35]. The BVS is the sum of S_{ij} , which is expressed as follows [36].

$$\text{BVS} = \sum_j S_{ij}. \quad \dots (4)$$

The values of the BVS for the Sn and O of SnNb₂O₆ and Sn₂Nb₂O₇ are summarized in Table 2. The R_{ij} ($< 3 \text{ \AA}$) values, which were evaluated from the crystal structure data of the *p*-type samples refined by the Rietveld analysis, are summarized in Table S3 (see supplementary section S5). The BVS of the Sn of SnNb₂O₆ is higher than that of Sn₂Nb₂O₇, suggesting that the Sn and O are tightly bonded in SnNb₂O₆ as compared to that in Sn₂Nb₂O₇.

Table 2. Bond valence sum (BVS) of the SnNb₂O₆ and Sn₂Nb₂O₇.

SnNb ₂ O ₆		Sn ₂ Nb ₂ O ₇	
atom	BVS	atom	BVS
O1	1.90	O1	1.57
O2	1.95	O2	1.93
O3	1.89		
Sn	2.37	Sn	1.54

Another indicator for the Sn-O bond strength is Debye temperature (θ_D), which is based on the amplitude of thermal vibration [37]. We estimated θ_D of Sn²⁺ for *p*-type SnNb₂O₆ and Sn₂Nb₂O₇ by means of ¹¹⁹Sn Mössbauer spectroscopy. Based on the high-temperature approximation of the Debye model, the Debye temperature is expressed with recoil-free fractions $f(T)$ as follows [38],

$$\ln f(T) = -6E_R T / k_B \theta_D^2, \quad \dots (5)$$

$$A = \text{const.} \times f, \quad \dots (6)$$

where A , θ_D , T , k_B , and E_R are the integral absorption intensity of Mössbauer peak, Debye temperature, measurement temperature, Boltzmann constant, and recoil energy, respectively. The temperature dependence of $\ln A$ and the estimated values of θ_D are shown in Fig. 4 (details are provided

in supplementary section S6). The slope of $\text{Sn}_2\text{Nb}_2\text{O}_7$ was larger than that of SnNb_2O_6 ; Therefore, the θ_D value of SnNb_2O_6 (237 K) was higher than that of $\text{Sn}_2\text{Nb}_2\text{O}_7$ (174 K). This is qualitatively in good agreement with the results obtained through the BVS estimations.

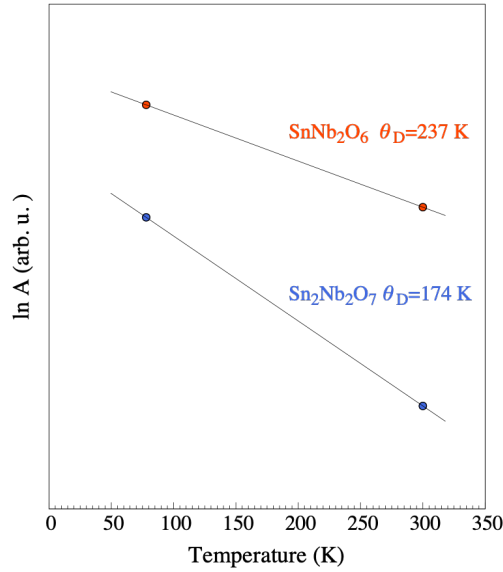


Figure 4. Temperature dependence of $\ln A$ obtained through the ^{119}Sn Mössbauer spectra and Debye temperature θ_D of Sn^{2+} sites for SnNb_2O_6 and $\text{Sn}_2\text{Nb}_2\text{O}_7$.

Comparing local structures around the Sn ions

Finally, we will discuss the origin of the differences in the Sn-O bond strengths of SnNb_2O_6 and $\text{Sn}_2\text{Nb}_2\text{O}_7$ by focusing on the local structures around the Sn ions. It is known that Sn $5s^2$ electrons have an asymmetric electron density and a large volume as same as that of oxygen ions [23]. Moreover, they act like the lone electron pair in the Sn^{2+} oxides [39,40]. The polarization of the $5s^2$ electrons occurs due to the hybridization of Sn $5s$ with O $2p$ and Sn $5p$ orbitals [39]. The schematic images of the local structures around the Sn ions of SnNb_2O_6 and $\text{Sn}_2\text{Nb}_2\text{O}_7$ are shown

in Fig. 5. In the case of SnNb_2O_6 , eight oxygen ions are arranged at the vertices of a square antiprism with the Sn ion at the center. The distance between Sn and O2 is large ($>3 \text{ \AA}$); therefore, there is a large space present toward the O2 side. The Sn $5s^2$ electrons can exist in space with a small steric hindrance. However, in the “ideal pyrochlore” structure of $\text{Sn}_2\text{Nb}_2\text{O}_7$, Sn is surrounded by eight closely arranged oxygen ions. To form an ideal pyrochlore structure, the defects and/or disorders are necessary [19-24] because large electrostatic repulsions occur between the Sn $5s^2$ electrons and oxygen ions. Considering the characteristic crystal structure geometry of $\text{Sn}_2\text{Nb}_2\text{O}_7$, the V_{O} formation at the O1 site could provide the space for the asymmetric electron density of Sn^{2+} . This led to a large amount of V_{O} formation for $\text{Sn}_2\text{Nb}_2\text{O}_7$, particularly around the Sn ions. Therefore, we can interpret the reason for the lower hole-generation efficiency of $\text{Sn}_2\text{Nb}_2\text{O}_7$ as compared to SnNb_2O_6 based on the characteristic crystal geometry.

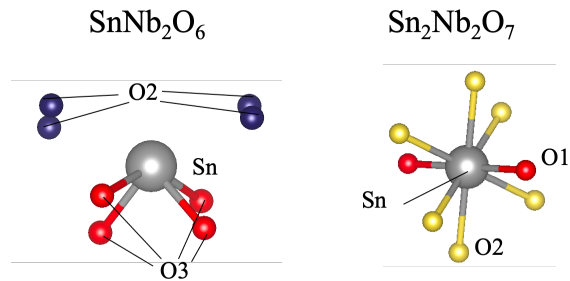


Figure 5 Schematic image of the local structure around the Sn ions of SnNb_2O_6 (left) and $\text{Sn}_2\text{Nb}_2\text{O}_7$ (right).

CONCLUSIONS

In conclusion, we investigated the oxygen vacancy ($V_{\text{O}}^{\cdot\cdot}$) formation in *p*-type SnNb_2O_6 and $\text{Sn}_2\text{Nb}_2\text{O}_7$ to reveal the origin of the differences in the hole-generation efficiencies η_{Hole} . The EXAFS spectra and Rietveld analysis indicated the preferential $V_{\text{O}}^{\cdot\cdot}$ formation at the oxygen sites, which were bonded to Sn ions in both the Sn-Nb complex oxides. Moreover, a larger amount of $V_{\text{O}}^{\cdot\cdot}$ formation was observed in $\text{Sn}_2\text{Nb}_2\text{O}_7$ with low η_{Hole} as compared to SnNb_2O_6 with high η_{Hole} . The difference in the $V_{\text{O}}^{\cdot\cdot}$ formations was due to the Sn-O bond strength, which is correlated with the local structure of Sn^{2+} and the asymmetric electron density of the Sn $5s^2$ electrons. Conversely, the distorted structure around the Sn ions and the long Sn-O bond length, such as those of SnNb_2O_6 , resulted in higher η_{Hole} through the suppression of $V_{\text{O}}^{\cdot\cdot}$ formation. Because such a structure has a large space for the Sn $5s^2$ electrons, it reduced the large electrostatic repulsions between the Sn $5s^2$ electrons and oxygen ions. To date, the development of *p*-type oxide which has *s*-orbital based VBM (*s*-orbital-based *p*-type oxide) has been limited because of the difficulty in controlling the formations of $V_{\text{O}}^{\cdot\cdot}$. Our data suggest the importance of the local structure around the Sn ions to prevent the $V_{\text{O}}^{\cdot\cdot}$ formations in the *p*-type Sn^{2+} -based complex oxides. Moreover, this approach is potentially adapted for other oxides with ns^2 cations (such as Pb^{2+} and Bi^{3+}) because they have similar ns^2 electrons with the asymmetric electron density and large volume. The findings in this study give us new direction for exploring a candidate of *s*-orbital-based *p*-type oxides through a reduction of the scattering center generated by structural defect formations.

ASSOCIATED CONTENT

Supporting Information

The supporting information is available free of charge on the ACS Publication website.

XRD patterns of SnNb_2O_6 and $\text{Sn}_2\text{Nb}_2\text{O}_7$, *FEFF* calculations of Sn K-edge and Nb K-edge EXAFS of SnNb_2O_6 , Summary of Rietveld analysis of *n*-type SnNb_2O_6 , Structural parameters of $\text{Sn}_2\text{Nb}_2\text{O}_7$ of O1 and O2 deficient model for calculated XRD patterns, Sn-O bond length of *p*-type SnNb_2O_6 and $\text{Sn}_2\text{Nb}_2\text{O}_7$, Mössbauer spectra and calculation of Debye temperature (PDF)

AUTHOR INFORMATION

Corresponding Author

Akane Samizo – Tokyo University of Science, Katsushika, Japan; orcid.org/0000-0002-7488-385X; E-mail : a-samizo@rs.tus.ac.jp

Author

Makoto Minohara – National Institute of Advanced Industrial Science and Technology (AIST), Tsukuba, Japan; orcid.org/0000-0003-4367-9175

Naoto Kikuchi – National Institute of Advanced Industrial Science and Technology (AIST), Tsukuba, Japan; orcid.org/0000-0003-1035-3515

Kyoko K. Bando – National Institute of Advanced Industrial Science and Technology (AIST), Tsukuba, Japan

Yoshihiro Aiura – National Institute of Advanced Industrial Science and Technology (AIST), Tsukuba, Japan; orcid.org/0000-0002-4478-7680

Ko Mibu – Nagoya Institute of Technology, Nagoya, Japan; orcid.org/0000-0002-6416-1028

Keishi Nishio – Tokyo University of Science, Katsushika, Japan

Author contributions

A.S., N.K., K.N. planned the whole experiments. A.S., M.M., N.K., K.K.B., Y.A. carried out

EXAFS measurements. A.S., N.K., K.N. performed Rietveld analysis and XRD measurements. K.M. and A.S. carried out ^{119}Sn Mössbauer spectroscopy measurements and performed the analysis of the spectra. A.S. wrote the paper with input from all co-authors.

Notes

The authors declare no competing financial interest.

ACKNOWLEDGMENTS

This work was supported by a Grant-in-Aid for Scientific Research (20K22472, 18K05285) from the Japan Society for the Promotion of Science (JSPS), and Tokyo University of Science (TUS) Grant for Young and Female Researchers. The work at KEK-PF was performed under the approval of the Program Advisory Committee (Proposals No. 2018G685, 2019G070, 2019G543, 2020G657) at the Institute of Materials Structure Science, KEK. We also thank Dr. Hiroaki Nitani for his technical support on the EXAFS measurements. The Mössbauer measurements were conducted at Nagoya Institute of Technology, supported by the Nanotechnology Platform Program (Molecule and Material Synthesis) of the Ministry of Education, Culture, Sports, Science and Technology (MEXT), Japan. We would like to thank Editage (www.editage.com) for English language editing.

REFERENCES

- [1] Nomura, K.; Ohta, H.; Takagi, A.; Kamiya, T.; Hirano, M.; Hosono, H. Room-temperature fabrication of transparent flexible thin-film transistors using amorphous oxide semiconductors. *Nature*, 2004, 432, 488–492.
- [2] Coll, M.; et al. Towards Oxide Electronics: A Roadmap. *Appl.Surf. Sci.* 2019, 482, 1–93.

- [3] Kawazoe, H.; Yanagi, H.; Ueda, K.; Hosono, H. Transparent *p*-Type Conducting Oxides: Design and Fabrication of *p-n* Heterojunctions. *MRS Bull.* 2000, 25, 28-36.
- [4] Hautier, G.; Miglio, A.; Ceder, G.; Rignanese, G.-M.; Gonze, X. Identification and Design Principles of Low Hole Effective Mass *P*-type Transparent Conducting Oxides. *Nat. Commun.* 2013, 4, 2292.
- [5] Zhang, K. H. L.; Xi, K.; Blamire, M. G.; Egdell, R. G. *P*-type Transparent Conducting Oxides. *J. Phys.: Condens. Matter* 2016, 28, 383002.
- [6] Wang, Z.; Nayak, P. K.; Caraveo-Frescas, J. A.; Alshareef, H. N. Recent Developments in *p*-Type Oxide Semiconductor Materials and Devices. *Adv. Mater.* 2016, 28, 3831–3892.
- [7] Bhatia, A.; Hautier, G.; Nilgianskul, T.; Miglio, A.; Sun, J.; Kim, H. J.; Kim, K. H.; Chen, S.; Rignanese, G. M.; Gonze, X.; Suntivich, J. High-Mobility Bismuth-based Transparent *p*-Type Oxide from High-Throughput Material Screening. *Chem. Mater.* 2016, 28, 30–34.
- [8] Ogo, Y.; Hiramatsu, H.; Nomura, K.; Yanagi, H.; Kamiya, T.; Hirano, M.; Hosono, H. *P*-Channel Thin-Film Transistor Using *P*-type Oxide Semiconductor, SnO. *Appl. Phys. Lett.* 2008, 93, 032113.
- [9] Ogo, Y.; Hiramatsu, H.; Nomura, K.; Yanagi, H.; Kamiya, T.; Hirano, M.; Hosono, H. Tin Monoxide as an s-Orbital-Based *P*-type Oxide Semiconductor: Electronic Structures and TFT Application. *Phys. Status Solidi A* 2009, 206, 2187-2191.
- [10] Minohara, M.; Kikuchi, N.; Yoshida, Y.; Kumigashira, H.; Aiura, Y. Improvement of the hole mobility of SnO epitaxial films grown by pulsed laser deposition. *J. Mater. Chem. C* 2019, 7, 6332–6336.

- [11] Minohara, M.; Samizo A.; Kikuchi, N.; Bando K. K.; Yoshida Y.; Aiura, Y. Tailoring the Hole Mobility in SnO Films by Modulating the Growth Thermodynamics and Kinetics. *J. Phys. Chem. C*. 2020, 124, 1755-1760.
- [12] Kikuchi, N.; Samizo, A.; Ikeda, S.; Aiura, Y.; Mibu, K.; Nishio, K. Carrier Generation in a P-type Oxide Semiconductor: $\text{Sn}_2(\text{Nb}_{2-x}\text{Ta}_x)\text{O}_7$. *Phys. Rev. Mater.* 2017, 1, 021601.
- [13] Samizo, A.; Kikuchi, N.; Aiura, Y.; Nishio, K.; Mibu, K. Carrier Generation in p-Type Wide-Gap Oxide: SnNb_2O_6 Foordite. *Chem. Mater.* 2018, 30, 8221–8225.
- [14] Samizo, A.; Kikuchi, N.; Nishio, K. Effect of Crystal Structure on Hole Carrier Generation in Wide-gap P-type Tin-Niobate. *MRS Adv.* 2019, 4, 1, 27-32.
- [15] Hosogi, Y.; Shimodaira, Y.; Kato, H.; Kobayashi, H.; Kudo, A. Role of Sn^{2+} in the Band Structure of SnM_2O_6 and $\text{Sn}_2\text{M}_2\text{O}_7$ (M = Nb and Ta) and Their Photocatalytic Properties. *Chem. Mater.* 2008, 20, 1299–1307.
- [16] Aiura Y.; Ozawa K.; Hase I.; Bando K. K.; Haga H.; Kawanaka H.; Samizo A.; Kikuchi N.; Mase K. Disappearance of Localized Valence Band Maximum of Ternary Tin Oxide with Pyrochlore Structure, $\text{Sn}_2\text{Nb}_2\text{O}_7$. *J. Phys. Chem. C* 2017, 121, 9480-9488.
- [17] Katayama, S.; Hayashi, H.; Kumagai, Y.; Oba, F.; Tanaka, I. Electronic Structure and Defect Chemistry of Tin(II) Complex Oxide SnNb_2O_6 . *J. Phys. Chem. C* 2016, 120, 9604–9611.
- [18] Chattopadhyay, D.; Queisser, H. J. ; Electron Scattering by Ionized Impurities in Semiconductors. *Rev. Mod. Phys.*, 1981, 53, 745-768.
- [19] Stewart, D. J; Knop, O.; , Meads, R. E.; Parker, W. G.; Pyrochlores. IX. Partially Oxidized $\text{Sn}_2\text{Nb}_2\text{O}_7$, and $\text{Sn}_2\text{Ta}_2\text{O}_7$: A Mössbauer Study of Sn(II,IV) Compounds. *Can. J. Chem.* 1973, 51, 1041-1049.

- [20] Subramanian, M. A.; Aravamudan, G.; Subba, Rao, G. V.; OXIDE PYROCHLORES – A REVIEW. *Prog. Solid State Chem.* 1983, 15, 55-143.
- [21] Birchall, T.; Sleight, A. W.; Nonstoichiometric Phases in the Sn-Nb-O and Sn-Ta-O Systems Having Pyrochlore-Related Structures. *J. Solid State Chem.* 1975, 13, 118-130.
- [22] Mizoguchi, H.; Wattiaus, A.; Kykyneshi, R.; Tate, J.; Sleight, A. W.; Subramanian, M. A. Synthesis and Characterization of Sn²⁺ Oxides with the Pyrochlore Structure. *Mater. Res. Bull.* 2008, 43, 1943-1948.
- [23] Cruz, L. P.; Savariault, J. -M.; Rocha, J. Pyrochlore-Type Tin Niobate. *Acta Cryst. Sect. C*, 2001, 57, 1001-1003.
- [24] Cruz, L. P.; Savariault, J. -M.; Rocha, J.; Jumas, J. -C.; Pedrosa de Jesus J. D., Synthesis and Characterization of Tin Niobates. *J. Sol. St. Chem.* 2001, 156, 349-354.
- [25] Izumi, F.; Momma, K. Three-Dimensional Visualization in Powder Diffraction. *Sol. St. Phenom.* 2007, 130, 15–20.
- [26] Momma, K.; Izumi, F. VESTA 3 for Three-Dimensional Visualization of Crystal, Volumetric and Morphology Data *J. Appl. Crystallogr.* 2011, 44, 1272-1276.
- [27] Nomura, M.; Koike, Y.; Sato, M.; Koyama, A.; Inada, Y.; Asakura, K. A New XAFS Beamline NW10A at the Photon Factory. *AIP Conf. Proc.* 2007, 882, 896.
- [28] Ravel, B.; Newville, M. ATHENA, ARTEMIS, HEPHAESTUS: Data Analysis for X-ray Absorption Spectroscopy Using IFEFFIT. *J. Synchrotron Radiat.* 2005, 12, 537–541.
- [29] Zabinsky, S. I.; Rehr, J. J.; Ankudinov, A.; Albers R. C.; Eller M. J. Multiple-Scattering Calculations of X-ray-Absorption Spectra, *Phys. Rev. B* 1995, 52, 2995.

- [30] Ankudinov, A. L.; Ravel, B.; Rehr, J. J.; Conradson, S. D. Real-Space Multiple-Scattering Calculation and Interpretation of X-ray-Absorption Near-Edge Structure, *Phys. Rev. B* 1998, 58, 7565.
- [31] Brown, I. D.; Shannon, R.D.; Empirical Bond-Strength-Bond-Length Curves for Oxides. *Acta Cryst.* 1973, A29, 266-282.
- [32] Wang, X.; Liebau, F.; Influence of Lone-Pair Electrons of Cations on Bond-Valence Parameters. *Z. Kristallogr.* 1996, 211, 437-439.
- [33] Wang, X. The Contribution To Bond Valences By Lone Electron Pairs. *Mater. Res. Soc. Symp. Proc.* 2005, 848, FF7.4.1.
- [34] Brese, N. E.; O'Keeffe, M., Bond-Valence Parameters for Solids. *Acta Cryst B.* 1991, 47, 192-197.
- [35] Tytko, K. H.; Mehmke, J.; Kurad D. Bond Length-bond Valence Relationships with Particular Reference to Polyoxometalate Chemistry. In: Bard A.J. et al. (eds) *Bonding and Charge Distribution in Polyoxometalates: A Bond Valence Approach. Structure and Bonding*, vol 93. 1999, Springer, Berlin, Heidelberg.
- [36] Camargo, P.H.C.; Brown, I. D. The Chemical Bond in Inorganic Chemistry: the Bond Valence Model, 2nd ed. *J. Mater. Sci.* 2017, 52, 9959–9962.
- [37] Jiang, D.; Wu, M.; Liu, D.; Li, F.; Chai, M.; Liu, S. Structural Stability, Electronic Structures, Mechanical Properties and Debye Temperature of Transition Metal Impurities in Tungsten: A First-Principles Study. *Metals* 2019, 9, 967.
- [38] Gütlich, P. H.; Link, R.; Trautwein, A. *Mössbauer Spectroscopy and Transition Metal Chemistry.* 1978, Springer-Verlag, Berlin.

[39] Walsh, A.; Payne, J. D.; Egdell G. R.; Watson, W. G.; Stereochemistry of Post-Transition Metal Oxides: Revision of the Classical Lone Pair Model. Chem. Soc. Rev. 2011, 40, 4455-4463.

[40] Galy, J.; Meunier, G.; Anderson, S.; Åatröm, A.; Stéréochimie des éléments comportant des paires non liées: Ge (II), As (III), Se (IV), Br (V), Sn (II), Sb (III), Te (IV), I (V), Xe (VI), Tl (I), Pb (II), et Bi (III) (oxydes, fluorures et oxyfluorures). J. Sol. St. Chem. 1975, 13, 142-159.

Insert Table of Contents artwork here

